Propellant-Optimal Powered Descent Guidance

Ping Lu*

San Diego State University, San Diego, California 92182-1308

The problem of guiding a rocket-powered vehicle to land on a planet (or the Moon) with pinpoint precision and minimum propellant usage is the focus of this work. Three related but different versions of optimal powered descent problems are formulated with different intended purposes. Comparison and relationships among the solutions to these problems are analyzed. A theoretical investigation reveals the detailed structure of the optimal thrust magnitude profile in the problems, and helps significantly simplify the design of the guidance algorithm. An indirect-method-based fast and robust algorithm is developed to solve these problems. Another unique contribution of this paper is a novel and simple strategy to adaptively determine on-board a desirable powered descent initiation condition so that no major divert is required of the powered descent trajectory. The algorithm is demonstrated in closed-loop simulations for a human Mars mission where a significantly heavier landing mass and more stringent landing precision are required than in any robotic missions thus far.

I. Introduction

Powered descent refers to a phase in a planetary landing mission where the rocket provides the necessary retro-propulsion and steering of the trajectory to meet the required terminal condition, either at the landing site or above the landing site. Powered descent guidance determines the thrust vector direction, thrust magnitude, and engine burn time in this phase. The Apollo lunar descent guidance [1–3] exemplifies the existing technology. In Apollo descent guidance literature, the thrust acceleration vector is represented by a linear function of time (called E-guidance [1]) if only the terminal position and velocity are specified, and a quadratic function [2] if the terminal position,

*Professor and Chair, Department of Aerospace Engineering; plu@sdsu.edu, Fellow AIAA

velocity, and acceleration are prescribed (which was the version of Apollo lunar descent guidance flown). The coefficients of the polynomials are determined by satisfying the specified terminal conditions. In the original design, the polynomial representations are chosen for simplicity and comparatively good fuel performance (this what the term "optimizing" in Ref. [1] means). Later it is discovered that the E-guidance solution actually is the optimal solution for a descent problem with final position and velocity specified, if a *quadratic* performance index on the acceleration vector is minimized. [4] No similar finding on the quadratic polynomial solution is known yet. Note that minimizing a quadratic performance index is not equivalent to minimizing propellant consumption (which requires a performance index of the 2-norm of the acceleration vector).

With the benefit of hindsight and over 4 decades of research since the Apollo era, we now have the luxury to point out some shortcomings of the Apollo descent guidance. One is propellant optimality. Apollo descent guidance is not propellant optimal (or "fuel-optimal" as used alternately in the literature). It has been reported that rocket trajectories optimal with respect to a performance index that is not exactly propellant usage can incur tens of percents more propellant consumption as compared to the fuel-optimal solution. [5] Evidence of propellant advantages of fuel-optimal guidance methods over Apollo descent guidance is reported more recently in Ref. [6]. For a future human Mars mission, a landing mass is required that is easily tens of times that of a robotic mission. Propellant optimality in powered descent for such a heavy mission is a critical factor affecting the feasibility of the mission. Moreover, the Apollo descent guidance design does not take into account the hard upper and lower bounds on the thrust magnitude, and the commanded thrust magnitude can be outside the capability of the engine, which may impact adversely the landing precision. Finally Apollo descent guidance solution requires a specified time of flight. While an initial value of the time of flight can be chosen off-line by trials in a relatively wide range, and various approaches have been proposed to compute it, [2, 4, 7] a better propellant performance is typically associated with a shorter time of flight. But such a value is not easy to determine on-board.

In the last 20 years, there has been a renewed interest in investigating powered descent guidance algorithms and trajectory optimization, much of which is motivated by robotic Mars missions. [4, 7–18] Among these existing works, the most relevant to this paper are the 3-dimensional (3-

D) fuel-optimal control problem and method of solution in Ref. [15], and the Guidance for Fuel Optimal Large Divert (G-FOLD) in Refs. [12, 13, 16–18]. Analytical solutions along maximum or minimum (*constant*) thrust-acceleration arcs are developed in Ref. [15], and the numerical solution to the fuel-optimal problem is reduced to a two-parameter search problem. To apply the method for guidance purposes though, some efficient way is still needed to determine the optimal burn time of each constant thrust-acceleration arc. G-FOLD solves the fixed-time, 3-D fuel-optimal descent problem subject to realistic trajectory constraints such as those on upper and lower bounds on the thrust magnitude, glide slope, thrust-vector pointing direction, and others. The numerical solution is obtained by a *direct* method that solves a second-order cone program (SOCP). A customized interior-point algorithm is developed for on-board solution of the SOCP. [18]

A three-dimensional propellant-optimal powered descent guidance algorithm based on the *indirect* method is developed in this paper. The basic tenet of the algorithm rests on a more general rocket powered guidance methodology, dubbed Universal Powered Guidance (UPG), that has been developed over the years by the author and applied to ascent, deorbit, and orbital transfers. [19–22] This powered-descent version of UPG is originally developed in the author's work in technology development for human Mars missions where a much heavier landing mass and at least one order of magnitude higher landing precision are required than any robotic missions flown thus far. The final product of the guidance algorithm however is applicable to human or robotic missions in planetary or Moon landing. This descent algorithm will be called UPG for short herein.

When solving a fuel-optimal flight problem with a throttlable rocket by the indirect method, a major challenge is to determine the thrust magnitude profile. The switching function theory is useful in analyzing and understanding the problem, but not for reliable numerical solutions. An analysis is conducted in this paper to ascertain the structure (bang-bang magnitude and the number of switches) of the thrust profile in a three-dimensional fuel-optimal powered descent problem. UPG will then find the optimal burn times of the subarcs. The advantages as compared to G-FOLD are that the UPG code is simpler and much less computationally intensive, the algorithm provides the optimal burn time as a part of the solution, and it accommodates different problem formulations and terminal constraints that may not be readily suitable for SOCP formulation (e.g.,

see Section II-C). The disadvantages include that inequality constraints such as those on glide slope and thrust pointing direction are difficult to enforce by UPG, and the algorithm does not enjoy theoretically guaranteed convergence and polynomial complexity. On balance, the UPG algorithm developed in this paper and G-FOLD complement each other, and each is potentially more suited for certain application scenarios.

This paper also addresses an important problem that is not discussed in most of existing works, that is, how to determine in-flight an appropriate condition to commence the powered descent phase? The existing literature on powered descent guidance implicitly assumes that the start of the powered descent phase is triggered externally (for instance, by a prescribed time, altitude or velocity). Powered descent guidance is just a passive recipient of the initial condition. A novel technique is developed in this paper to use a particular capability of UPG to predict when is best to initiate the powered descent phase. This strategy ensures that the powered descent phase starts at a condition that results in little divert requirement, even in the presence of significant trajectory dispersions prior to the powered descent phase. In this way the vehicle need not maneuver aggressively during powered descent and the probability for pinpoint landing is further enhanced.

The theoretical investigation and method of solution employed in the guidance algorithm are presented in the rest of this paper. The various aspects of the development and the functionalities of UPG are demonstrated by closed-loop simulations of a human Mars mission that involves lifting entry and powered descent to landing by a supersonic retro-propulsion system.

II. Optimal Powered Descent Problems

A. General Problem

In a Cartesian coordinate system with the origin at the center of mass of the planet, the three-dimensional point-mass equations of motion for a rocket-powered vehicle can be written as

$$\dot{\boldsymbol{r}} = \boldsymbol{V} \tag{1}$$

$$\dot{\boldsymbol{V}} = \boldsymbol{g}(\boldsymbol{r}) + \frac{T}{m(t)}\mathbf{1}_T(t) \tag{2}$$

$$\dot{m} = -\frac{T}{v_{ex}} \tag{3}$$

where the planet is either assumed to have no atmosphere, or the atmosphere is sufficiently thin to be ignorable in the powered descent guidance solution. The rocket engine thrust has a magnitude T and $\mathbf{1}_T$ is the *unit* vector that defines the thrust direction. The direction of $\mathbf{1}_T$ generally changes with time, and T is allowed to vary as well. The effective exhaust velocity of the rocket engine v_{ex} is considered a constant. The vectors $\boldsymbol{r} \in R^3$ and $\boldsymbol{V} \in R^3$ are the position and inertial velocity vector of the vehicle with the current mass m.The gravitational acceleration $\boldsymbol{g}$ is a function of $\boldsymbol{r}$, and it has a magnitude of g_0 at the equatorial radius of the planet R_0. A constant gravity simplification for planetary landing guidance is well justified for relatively short flight, and we will use this assumption in an analysis in Section V-A later. In our algorithm implementation a central gravity model is actually retained because (a) it does not add any additional difficulty to our approach; (b) a significant part of the powered descent guidance software can share the functions/subroutines with other guidance functionalities of UPG for ascent, deorbit, and orbital transfer applications where constant gravity is not a valid simplification; and (c) the descent guidance algorithm will remain applicable for longer powered descent (such as landing on the Moon or a planet without atmosphere) where the direction of the gravity vector can change substantially.

The initial state is assumed to be specified and T and $\mathbf{1}_T$ are constrained

$$\boldsymbol{r}(t_0) = \boldsymbol{r}_0, \qquad \boldsymbol{V}(t_0) = \boldsymbol{V}_0, \qquad m(t_0) = m_0 \tag{4}$$

$$T_{min} \leq T(t) \leq T_{max} \tag{5}$$

$$\|\mathbf{1}_T(t)\| = 1 \tag{6}$$

where $T_{min} \geq 0$ and $T_{max} \geq T_{min}$ are constant. The powered descent problem is to determine the thrust magnitude profile $T(t)$ and the thrust direction $\mathbf{1}_T(t)$, subject to Eqs. (5) and (6), so that the trajectory of the vehicle will start from the current condition in Eq. (4) and end at a point where a set of prescribed terminal conditions is met

$$\boldsymbol{s}[\boldsymbol{r}(t_f), \boldsymbol{V}(t_f), t_f] = \mathbf{0} \tag{7}$$

The constraints in Eq. (7) specify the condition the final position and velocity vectors should satisfy

for a particular landing scenario (see the following subsections). The *optimal* powered descent problem is one in which all the aforementioned conditions are met, and a performance index of the following form is minimized

$$J = \kappa\phi(\boldsymbol{r}_f, \boldsymbol{V}_f, t_f) + \varepsilon \int_0^{t_f} \frac{T}{v_{ex}} dt \tag{8}$$

where $\kappa \geq 0$ and $\varepsilon \geq 0$ are constants. This performance index includes essentially all commonly used optimization measures. For instance, if $\phi = 0$, this becomes a minimum-propellant problem for any $\varepsilon > 0$; if $\varepsilon = 0$ and $\phi = t_f$, this is a minimum-time problem for any $\kappa > 0$; still if $\varepsilon = 0$, $\kappa > 0$, and $\phi = \boldsymbol{V}^T(t_f)\boldsymbol{V}(t_f)$, it is a minimum-final-velocity problem. Depending on the specific forms of the terminal constraints in Eq. (7) and the performance index in Eq. (8), three different variations of the optimal powered descent problem are defined in the subsequent sections.

Unlike in the Apollo powered descent guidance where the flight time is specified, [1, 2] the final time t_f in our problem setting is free, to be found as a part of the optimal solution.

B. Pinpoint Landing Problem

Let $\boldsymbol{r}^* \in R^3$ be the specified vector that defines target position vector (e. g., the location of the landing site) and $\boldsymbol{V}^* \in R^3$ the vector that gives the target relative velocity with respect to the landing site. The terminal constraints in Eq. (7) in this problem take the specific form of

$$\boldsymbol{r}(t_f) = \boldsymbol{r}^* \tag{9}$$

$$\boldsymbol{V}(t_f) = \boldsymbol{V}^* \tag{10}$$

The performance index is just propellant consumption ($\kappa = 0$ and $\varepsilon = 1$ in Eq. (8))

$$J_1 = \int_0^{t_f} \frac{T}{v_{ex}} dt \tag{11}$$

This problem requires that the vehicle uses the least amount of propellant to terminate its descent precisely at the target position with the required relative velocity, hence the *pinpoint landing* prob-

lem.

C. Bolza Landing Problem

In this setting the vehicle is required to terminate at a specified altitude (or on the ground) with a specified relative velocity (vector). The terminal constraints are therefore now

$$\|\boldsymbol{r}(t_f)\| = \|\boldsymbol{r}^*\| \tag{12}$$

$$\boldsymbol{V}(t_f) = \boldsymbol{V}^* \tag{13}$$

where the 2-norm (Euclidean norm) is used in Eq. (12). The condition in Eq. (12) suggests that the final altitude is equal to the required one, but the landing location may be different from the one specified by the vector $\boldsymbol{r}^*$. To put a penalty on the landing position error $\boldsymbol{r}(t_f) - \boldsymbol{r}^*$, the performance index is modified to be

$$J_2 = \kappa \left[\boldsymbol{r}(t_f) - \boldsymbol{r}^*\right]^T \left[\boldsymbol{r}(t_f) - \boldsymbol{r}^*\right] + \int_0^{t_f} \frac{T}{v_{ex}} dt, \quad \kappa > 0 \tag{14}$$

where $\kappa > 0$ is a constant (and the constant $\varepsilon = 1$ as compared to Eq. (8)). We call this the *Bolza* landing problem because an optimal control problem with a composite performance index of an integral plus a term dependent only on the final state is called a Bolza problem.

A main reason for considering this problem is for the case where there is no feasible solution to satisfy both the final position and velocity constraints in Eqs. (9) and (10) in the pinpoint-landing problem. This would happen when the divert requirement is beyond the capability of the vehicle, either due to large trajectory dispersions or contingencies such as partial failure of the retro-propulsion system. In such a case it may be desired to land the vehicle softly and as closely as possible to the designated landing site, without excessive propellant usage.

The Bolza problem formulation also has a numerical advantage. The terminal state of the preceding pinpoint-landing problem is tightly constrained to a single point in the sate space. The problem thus can cause convergence challenges if the initial condition is near the boundary of the feasible region. The Bolza landing problem posed here allows the terminal state to lie on a two-

dimensional manifold in the state space, rendering the search process for the solution significantly easier. Consequently numerical convergence of the Bolza landing problem is more robust (provided that κ is not exceedingly large). A more detailed discussion on the effects of the coefficient κ and the relationship between the pinpoint-landing and Bolza landing problems will be given in Section III later.

D. Soft Landing Problem

This problem has the same terminal constraints as in the Bolza landing problem

$$\|\boldsymbol{r}(t_f)\| = \|\boldsymbol{r}^*\| \tag{15}$$

$$\boldsymbol{V}(t_f) = \boldsymbol{V}^* \tag{16}$$

However the performance index is only propellant consumption (i. e., when $\kappa = 0$ in Eq. (14)):

$$J_3 = \int_0^{t_f} \frac{T}{v_{ex}} dt \tag{17}$$

In this problem the objective is to softly land on the ground with the minimum propellant usage, regardless of where the actual landing location is. There is no divert requirement to reach a specified location. The guidance focuses on reducing the velocity to the required value when the vehicle touches down. Not surprisingly, the trajectory maneuvers are benign and gentle, and the trajectory is close (but not identical) to the gravity-turn trajectory which is one where the thrust vector is always pointed to the negative direction of the velocity vector. Obviously the solution to the pinpoint-landing problem is a feasible solution to the soft-landing problem (meaning that the pinpoint-landing solution satisfies all the constraints in the soft-landing problem), but the reverse is generally not true. Therefore the propellant usage by the soft-landing trajectory is in all likelihood smaller, but most certainly no greater, than that by the pinpoint-landing trajectory. More discussion regarding propellant usage comparison is in Section III.

The soft-landing problem provides an appealing alternative for emergence landing in the event of partial propulsion system failure or other contingencies when the vehicle's ability to steer is im-

paired and landing on or close to the designated site(s) is no longer possible. But more importantly this formulation leads to a novel technique to determine when to start the powered descent, which will be discussed in Section VI later.

The UPG algorithm developed in this paper allows the options to solve any of the 3 versions of the optimal powered descent problems defined in the subsections of B-D of Section II.

III. Analysis of Optimal Powered Descent Problems

In this section the effects of the coefficient κ in the performance index in Eq. (14) and the relationship among the Bolza landing problem in Section II-C, soft-landing problem in Section II-D, and pinpoint-landing problem in Section II-B are analyzed. The nature of the findings in this section is similar to what is seen in the penalty method in numerical optimization. [23] Nonetheless, this exercise is still quite instructive in understanding how κ drives the landing error $\boldsymbol{r}(t_f) - \boldsymbol{r}^*$ with performance index in Eq. (14) and the propellant usage comparison in these 3 optimal powered descent problems. In the rest of this section it is understood that the initial condition, engine parameters, and $\boldsymbol{r}_f^*$ and $\boldsymbol{V}_f^*$ are the same in all the problems discussed.

Let $0 \leq \kappa_1 < \kappa_2 < \cdots < \kappa_n < \kappa_{n+1} < \cdots$ be a sequence of values for the weighting coefficient κ. Assume that for each κ_n the Bolza landing problem has a solution. Let $\boldsymbol{z}_n^* = (\boldsymbol{u}_n^*(t), \boldsymbol{x}_n^*(t), t_{f_n}^*)$ represent the solution to the Bolza landing problem in Section II-C corresponding to $\kappa = \kappa_n$, including the control (T and $\mathbf{1}_T$), state, and final time. For each κ_n, denote the optimal value of the performance index in Eq. (14) by

$$J_2(\kappa_n, \boldsymbol{z}_n^*) = \kappa_n \left[\boldsymbol{r}_n^*(t_{f_n}^*) - \boldsymbol{r}^*\right]^T \left[\boldsymbol{r}_n^*(t_{f_n}^*) - \boldsymbol{r}^*\right] + \int_0^{t_{f_n}^*} \frac{T_n^*(t)}{v_{ex}} dt := \kappa_n e(\boldsymbol{z}_n^*) + p(\boldsymbol{z}_n^*) \tag{18}$$

where the definitions of the terms $e(\boldsymbol{z}_n^*)$ and $p(\boldsymbol{z}_n^*)$ are clear from Eq. (18): with the final altitude constraint in Eq. (12), $e(\boldsymbol{z}_n^*)$ is the square of the final position error from the desired landing site, and $p(\boldsymbol{z}_n^*)$ is the propellant usage along the trajectory. We have the following properties regarding the sequence of solutions.

Property 1

The landing position error in the Bolza landing problem with a larger κ is smaller than or equal

to that with a smaller κ, that is

$$e(z^*_{n+1}) \leq e(z^*_n) \tag{19}$$

Proof: Since z^*_n gives the minimum value of the performance index in Eq. (18) with $\kappa = \kappa_n$, and z^*_{n+1} with $\kappa = \kappa_{n+1}$, we must have

$$\kappa_n e(z^*_n) + p(z^*_n) \quad \leq \quad \kappa_n e(z^*_{n+1}) + p(z^*_{n+1}) \tag{20}$$

$$\kappa_{n+1} e(z^*_{n+1}) + p(z^*_{n+1}) \quad \leq \quad \kappa_{n+1} e(z^*_n) + p(z^*_n) \tag{21}$$

Add Eqs. (20) and (21), cancel the like terms of $p(z^*_n)$ and $p(z^*_{n+1})$, and rearrange the rest of the terms to arrive at

$$(\kappa_{n+1} - \kappa_n) e(z^*_{n+1}) \leq (\kappa_{n+1} - \kappa_n) e(z^*_n) \tag{22}$$

Because $\kappa_{n+1} - \kappa_n > 0$, the above equation implies Eq. (19).

Property 1 states what is to be expected: with a larger κ, the landing position error in the Bolza landing problem is no greater (most likely smaller) than that with a smaller κ. The next property states that the propellant usage will (likely) increase with a larger κ.

Property 2

The propellant usage in the Bolza landing problem with a larger κ is greater than or equal to that with a smaller κ. Mathematically it is equivalent to

$$p(z^*_n) \leq p(z^*_{n+1}) \tag{23}$$

Proof:

Again because z^*_n yields the minimum of $J_2(\kappa, z) = \kappa e(z) + p(z)$ with $\kappa = \kappa_n$, this means

$$\kappa_n e(z^*_n) + p(z^*_n) \leq \kappa_n e(z^*_{n+1}) + p(z^*_{n+1}) \tag{24}$$

From Eq. (19) in Property 1, the left hand side of the preceding equation satisfies

$$\kappa_n e(z^*_{n+1}) + p(z^*_n) \leq \kappa_n e(z^*_n) + p(z^*_n) \tag{25}$$

Combining Eqs. (24) and (25) leads to

$$\kappa_n e(z^*_{n+1}) + p(z^*_n) \leq \kappa_n e(z^*_{n+1}) + p(z^*_{n+1}) \tag{26}$$

Canceling $\kappa_n e(z^*_{n+1})$ from both sides of the above equation gives the condition in Eq. (23).

Property 1 and 2 suggest that as κ increases in the performance index in Eq. (14) of the Bolza landing problem, the landing position error will (likely) decrease, and the propellant usage will (likely) increase. The increase in propellant usage is attributed to the additional divert maneuvers required to land the vehicle closer to the landing site (represented by $\boldsymbol{r}^*$).

Now we turn our attention to propellant usage in the 3 different formulations of the powered descent problem. Let $z^* = (\boldsymbol{u}^*(t), \boldsymbol{x}^*(t), t^*_f)$ represent the solution to the pinpoint-landing problem in Section II-B. The propellant usage comparison between the pinpoint-landing and Bolza landing problem is summarized in the next property.

Property 3

The propellant usage in the optimal pinpoint-landing problem is greater than or equal to that in the Bolza landing problem with any $\kappa \geq 0$, i. e., for $\kappa = \kappa_n$ with any $n \geq 0$,

$$p(z^*) \geq p(z^*_n) \tag{27}$$

Proof:

From the terminal constraints in Eq. (9) in the pinpoint-landing problem, we see that

$$e(z^*) = 0$$

Therefore

$$p(z^*) = \kappa_n e(z^*) + p(z^*) \geq \kappa_n e(z^*_n) + p(z^*_n) \tag{28}$$

The inequality in the above equation comes from the fact the z_n^* is minimizing with κ_n. Since $\kappa_n \geq 0$ and $e(z_n^*) \geq 0$, $\kappa_n e(z_n^*) + p(z_n^*) \geq p(z_n^*)$. Using this result in Eq. (28) proves Eq. (27)

It is possible to further prove on the basis of Properties 1–3 that the solution of the Bolza landing problem converges to the solution of the pinpoint-landing problem as $n \to \infty$ and $\kappa_n \to +\infty$. However we will not go through the exercise here. We trust that the reader will already see this as a logical conclusion.

Property 2 and 3 have a corollary as follows.

Property 4

The soft-landing problem incurs the least propellant usage among the three optimal powered descent problems in Sections II-B, II-C, and II-D.

Proof:

Since $\kappa = 0$ in the soft-landing problem, the propellant usage in the soft-landing problem is no greater than that in the Bolza landing problem with any $\kappa > 0$ by Property 2. The propellant usage in the Bolza landing problem on the other hand is no greater than that in the pinpoint-landing problem based on Property 3. Hence Property 4 follows.

IV. Method of Solution

In this section the numerical method to solve the problems posed in Section II is described.

A. Analytical Solution

Much of the material in this subsection can be found in the literature, e. g., Refs. [19, 22]. The following summary is presented for the convenience of the reader. Since the variations of the radius is small compared to the equatorial radius of the planet along the powered descent trajectory, the inverse-square gravitational acceleration can be approximated by a linear function of the radius vector [24]

$$\boldsymbol{g}(\boldsymbol{r}) = -\frac{\mu}{r^3}\boldsymbol{r} \approx -\frac{\mu}{{R_0}^3}\boldsymbol{r} := -\bar{\omega}^2\boldsymbol{r} \tag{29}$$

where μ is the gravitational parameter and $\bar{\omega} = \sqrt{\mu/{R_0}^3}$ is the Schuler frequency at R_0. Again for planetary powered descent a constant gravity field may be sufficient in the problem formulation.

But a central gravity field does not add any difficulty to our development.

For better numerical conditioning, the length is normalized by R_0, the velocity by $\sqrt{R_0 g_0}$, and the time by $\sqrt{R_0/g_0}$. With some abuse of notation, we still use $\boldsymbol{r}$ and $\boldsymbol{V}$ to denote the dimensionless position and velocity, and t for the dimensionless time. The dimensionless equations of motion are then [19]

$$\boldsymbol{r}' = \boldsymbol{V} \tag{30}$$

$$\boldsymbol{V}' = -\boldsymbol{r} + \frac{T}{m(t) g_0}\mathbf{1}_T \tag{31}$$

$$m' = -\frac{T}{v_{ex}}\sqrt{\frac{R_0}{g_0}} \tag{32}$$

The differentiation is with respect to the nondimensional time. For the performance indices in Eqs. (11), (14), and (17), the necessary conditions for the optimal control problem [25] calls for the Hamiltonian H

$$H = \boldsymbol{p}_r^T \boldsymbol{V} + \boldsymbol{p}_V^T\left(-\boldsymbol{r} + \frac{T}{m g_0}\mathbf{1}_T\right) - p_m \frac{T}{v_{ex}}\sqrt{\frac{R_0}{g_0}} - \frac{T}{v_{ex}}\sqrt{\frac{R_0}{g_0}} \tag{33}$$

where $\boldsymbol{p}_r \in R^3$, $\boldsymbol{p}_V \in R^3$, and $p_m \in R$ are the costate associated with $\boldsymbol{r}$, $\boldsymbol{V}$ and, m, respectively. The costate $\boldsymbol{p}_V$ and $\boldsymbol{p}_r$ satisfy the differential equations

$$\begin{pmatrix} \boldsymbol{p}_r' \\ \boldsymbol{p}_V' \end{pmatrix} = -\begin{pmatrix} \partial H/\partial \boldsymbol{r} \\ \partial H/\partial \boldsymbol{V} \end{pmatrix} = \begin{pmatrix} \boldsymbol{p}_V \\ -\boldsymbol{p}_r \end{pmatrix} \tag{34}$$

The optimal control theory [25] dictates that the optimal unit thrust direction vector is one that maximizes H, which leads to

$$\mathbf{1}_T = \boldsymbol{p}_V / \|\boldsymbol{p}_V\| \tag{35}$$

It will be formally stated in Section V-A and proven in the Appendix that the optimal thrust magnitude T for the powered descent problems will be either on the upper bound T_{max} or lower bound T_{min}, that is, a *bang-bang* profile. *Any intermediate thrust value in a finite interval is not*

optimal.

The analytical solutions to the costate equation (34) and solution to the state equations (30-31), first presented in Ref. [24], are given below for completeness. Suppose that the starting time for the powered trajectory is t_0. Let $\boldsymbol{p}_{V_0}$ and $\boldsymbol{p}_{r_0}$ are the (to-be-determined) initial conditions for the costate at t_0. Define

$$\boldsymbol{\lambda}(t) = \begin{pmatrix} \boldsymbol{p}_V(t) \\ -\boldsymbol{p}_r(t) \end{pmatrix}, \quad \boldsymbol{\lambda}(t_0) = \boldsymbol{\lambda}_0 = \begin{pmatrix} \boldsymbol{p}_{V_0} \\ -\boldsymbol{p}_{r_0} \end{pmatrix}$$

where t and t_0 are all nondimensional time. For $t \geq t_0$ the costate equation Eq. (34) has closed-form solution as a function of $\boldsymbol{\lambda}_0$

$$\boldsymbol{\lambda}(t) = \begin{bmatrix} \cos(t-t_0)I_3 & \sin(t-t_0)I_3 \\ -\sin(t-t_0)I_3 & \cos(t-t_0)I_3 \end{bmatrix} \boldsymbol{\lambda}_0 := \Phi(t-t_0)\boldsymbol{\lambda}_0 \tag{36}$$

where I_3 is a 3×3 unit matrix. Define the thrust integrals

$$\boldsymbol{i}_c(t,t_0) = \int_{t_0}^{t} \mathbf{1}_{p_V}(\tau)\cos(\tau)\frac{T}{m(\tau)g_0}d\tau \in R^3 \tag{37}$$

$$\boldsymbol{i}_s(t,t_0) = \int_{t_0}^{t} \mathbf{1}_{p_V}(\tau)\sin(\tau)\frac{T}{m(\tau)g_0}d\tau \in R^3 \tag{38}$$

where $\mathbf{1}_{p_V} = \boldsymbol{p}_V/\|\boldsymbol{p}_V\|$, and the mass m is a piecewise linear function of time, given that T is a piecewise constant as well as the mass rate. For a period where $T = T_{max}$ or $T = T_{min}$ and with solution of $\boldsymbol{p}_V$ from Eq. (36), the two thrust integrals can be evaluated accurately by a numerical quadrature formula (e. g., Simpson's rule or Milne's rule [19]), or by closed-form solutions if the burn time is not long [22]. In either case the thrust integrals in Eqs. (37) and (38) then become explicit linear functions of $\boldsymbol{p}_{V_0}$ and $\boldsymbol{p}_{r_0}$. [19, 22]

Let

$$\boldsymbol{x}(t) = \begin{pmatrix} \boldsymbol{r}(t) \\ \boldsymbol{V}(t) \end{pmatrix}, \quad \boldsymbol{x}_0 = \begin{pmatrix} \boldsymbol{r}_0 \\ \boldsymbol{V}_0 \end{pmatrix}, \quad \boldsymbol{i}(t,t_0) = \begin{bmatrix} \boldsymbol{i}_c(t,t_0) \\ \boldsymbol{i}_s(t,t_0) \end{bmatrix} \tag{39}$$

It can be easily verified that the state equations Eqs. (30) and (31) have the following solution

$$\boldsymbol{x}(t) = \Phi(t - t_0)\boldsymbol{x}_0 + \Gamma(t)\boldsymbol{i}(t, t_0) \tag{40}$$

where

$$\Gamma(t) = \begin{bmatrix} \sin(t)I_3 & -\cos(t)I_3 \\ \cos(t)I_3 & \sin(t)I_3 \end{bmatrix} \in R^{6\times 6} \tag{41}$$

For the specified initial state, the state $\boldsymbol{x}(t)$ at any $t > t_0$ is defined by Eq. (40) as a function of $\boldsymbol{p}_{V_0}$ and $\boldsymbol{p}_{r_0}$ through $\boldsymbol{i}(t, t_0)$. In summary, for any specified $t_f \geq t_0$ the state $\boldsymbol{x}(t_f)$ and costate $\boldsymbol{p}_V(t_f)$ and $\boldsymbol{p}_r(t_f)$ are (analytical) functions of the seven unknowns $\boldsymbol{z} = (\boldsymbol{p}_{V_0}^T \ \boldsymbol{p}_{r_0}^T \ t_f)^T \in R^7$. This conclusion applies to a trajectory with multi-burn arcs where the thrust magnitude takes different values (T_{max} or T_{min}) in each arc, provided that the burn time of each arc is given (except for the last one which is defined by the optimal t_f).

B. Nonlinear Algebraic System for the Solution

1. *Complete Conditions in Pinpoint Landing Problem*

For the pinpoint-landing problem in Section II-B, Eqs. (9)-(10) constitute 6 conditions on the unknown vector $\boldsymbol{z}$. The 7th condition comes from the transversality conditions in the optimal control theory [25] that $H(t_f) = 0$ for the free-time problem. Since $m(t_f)$ is not constrained, a transversality condition is $p_m(t_f) = 0$. Thus setting $H(t_f) = 0$ in Eq. (33) with $p_m(t_f) = 0$ gives the 7th condition

$$H(t_f) = \boldsymbol{p}_r^T(t_f)\boldsymbol{V}(t_f) - \boldsymbol{p}_V^T(t_f)\boldsymbol{r}(t_f) + \frac{T(t_f)}{m(t_f)g_0}\|\boldsymbol{p}_V(t_f)\| - \frac{T(t_f)}{v_{ex}}\sqrt{\frac{R_0}{g_0}} = 0 \tag{42}$$

where the optimal solution $\mathbf{1}_T = \boldsymbol{p}_V/\|\boldsymbol{p}_v\|$ has been used. An equivalent version of the condition in Eq. (42) that offers better numerical scaling is [19]

$$\boldsymbol{p}_r^T(t_f)\boldsymbol{V}(t_f) - \boldsymbol{p}_V^T(t_f)\boldsymbol{r}(t_f) + \frac{T(t_f)}{m(t_f)g_0}\|\boldsymbol{p}_V(t_f)\| = 1 \tag{43}$$

These 7 conditions (Eqs. (9)-(10) and (43)) constitute a root-finding problem of a system of 7 nonlinear algebraic equations for $\boldsymbol{z}$.

2. *Complete Conditions in Bolza and Soft Landing Problems*

For the Bolza landing problem in Section II-C (as well as the soft-landing problem in Section II-D) the terminal constraints in Eqs. (12) and (13) provide 4 final conditions. The transversality condition in Eq. (43) remains valid. The other 2 conditions will come from the transversality conditions associated the terminal constraints in the problem

$$\boldsymbol{p}(t_f) = -\kappa \frac{\partial \phi}{\partial \boldsymbol{x}_f} + \left[\frac{\partial \boldsymbol{s}(\boldsymbol{x}_f)}{\partial \boldsymbol{x}_f}\right]^T \boldsymbol{\nu} \tag{44}$$

where $\boldsymbol{p}(t_f) = (\boldsymbol{p}_r^T(t_f)\ \boldsymbol{p}_V^T(t_f))^T$, $\phi = \left[\boldsymbol{r}(t_f) - \boldsymbol{r}^*\right]^T \left[\boldsymbol{r}(t_f) - \boldsymbol{r}^*\right]$, $\boldsymbol{s}(\boldsymbol{x}_f) = 0$ represents the 4 constraints in Eqs. (12) and (13), and $\boldsymbol{\nu} \in R^4$ are constant multipliers. The unknown multipliers $\boldsymbol{\nu}$ may be eliminated amongst Eqs. (12), (13), and (44) to arrive at two equations involving only $\boldsymbol{x}(t_f)$ and $\boldsymbol{p}(t_f)$. These two equations are called *the reduced transversality conditions*. [26]. For the case in question here, the two reduced transversality conditions are given by [22]

$$\boldsymbol{y}_i^T(\boldsymbol{x}_f)\left(\boldsymbol{p}(t_f) + \kappa \frac{\partial \phi}{\partial \boldsymbol{x}_f}\right) = 0, \quad i = 1, 2 \tag{45}$$

where $\boldsymbol{y}_1 \in R^6$ and $\boldsymbol{y}_2 \in R^6$ are two linearly independent solutions of the following homogeneous linear system in $\boldsymbol{y} \in R^6$

$$\left[\frac{\partial \boldsymbol{s}(\boldsymbol{x}_f)}{\partial \boldsymbol{x}_f}\right] \boldsymbol{y} = \boldsymbol{0} \tag{46}$$

Note that such a solution $\boldsymbol{y}$ is clearly a function of $\boldsymbol{x}_f$. Since the 4 equations in $\boldsymbol{s}(\boldsymbol{x}_f) = 0$ (Eqs. (12) and (13)) are linearly independent, thus $\partial \boldsymbol{s}(\boldsymbol{x}_f)/\partial \boldsymbol{x}_f \in R^{4\times 6}$ has a rank of four, and the system of linear algebraic equations in $\boldsymbol{y}$ in Eq. (46) has two linearly independent solutions. Let

$$\boldsymbol{r}(t_f) = (r_{1_f}\ r_{2_f}\ r_{3_f})^T, \quad \boldsymbol{p}_r(t_f) = (p_{r_{1_f}}\ p_{r_{2_f}}\ p_{r_{3_f}})^T, \quad \boldsymbol{r}^* = (r_1^*\ r_2^*\ r_3^*)^T$$

Without loss of generality, we assume $r_{3_f} \neq 0$ (choose another nonzero-component and similar results can be readily obtained if $r_{3_f} = 0$). Then it can be shown that two independent solutions of Eq. (46) are

$$\boldsymbol{y}_1 = (1,\ 0,\ -r_{1_f}/r_{3_f},\ 0,\ 0,\ 0)^T, \quad \boldsymbol{y}_1 = (0,\ 1,\ -r_{2_f}/r_{3_f},\ 0,\ 0,\ 0)^T \tag{47}$$

And the two reduced transversality conditions from Eq. (45) are

$$r_{3_f} p_{r_{1_f}} - r_{3_f} p_{r_{1_f}} + \kappa(r_{1_f} r_3^* - r_{3_f} r_1^*) = 0 \tag{48}$$

$$r_{3_f} p_{r_{2_f}} - r_{2_f} p_{r_{3_f}} + \kappa(r_{2_f} r_3^* - r_{3_f} r_2^*) = 0 \tag{49}$$

Now the 7 equations in Eqs. (12), (13), (43), (48) and (49) provide the 7 equations for the 7 unknowns in $\boldsymbol{z}$ for the Bolza landing problem in Section II-C. Setting $\kappa = 0$ in Eqs. (48) and (49) yields the reduced transversality conditions for the soft-landing problem in Section II-D.

C. Numerical Implementation

The 7 nonlinear algebraic equations obtained in Section IV-B form a multi-variable root-finding problem where the unknown vector $\boldsymbol{z}$ is to be found to satisfy a system of 7 equations

$$\boldsymbol{f}(\boldsymbol{z}) = \boldsymbol{0} \tag{50}$$

While a number of possible numerical methods exist for solving the system in Eq. (50), such as the Newton-Raphson method, our finding is that the dogleg trust-region method by Powell [27] is the most robust in offering consistently reliable convergence for our problems, especially the pinpoint-landing problem where the Newton-Raphson method is prone to experiencing difficulty. Note that the vector function $\boldsymbol{f}$ in Eq. (50) has closed-form expression, and the Jacobian $\partial \boldsymbol{f}/\partial \boldsymbol{z}$ can also be analytically evaluated.

An initial guess $\boldsymbol{z}_0$ is required by the root-finding method in the very first solution of the problem. For the powered descent problem, the following choice of the initial costate for a "cold start"

is suggested

$$\boldsymbol{p}_{V_0}^{(0)} = -\frac{\boldsymbol{V}_0}{\|\boldsymbol{V}_0\|}, \quad \boldsymbol{p}_{r_0}^{(0)} = \boldsymbol{0} \tag{51}$$

The rationale for the choice of $\boldsymbol{p}_{V_0}^{(0)}$ rests with the conclusion that the direction of $\boldsymbol{p}_V$ is the direction of the optimal thrust vector (cf. Eq. (35)). For powered descent the thrust is likely to be nearly along the opposite direction of the velocity vector, i. e., $\boldsymbol{p}_V \approx -c(t)\boldsymbol{V}$ with a coefficient $c(t) > 0$. The selection of $c(t_0) = 1/\|\boldsymbol{V}_0\|$ in Eq. (51) simply provides a desirable scaling of $\boldsymbol{p}_{V_0}^{(0)}$. The choice of $\boldsymbol{p}_{r_0}^{(0)}$ is somewhat arbitrary. But since $\boldsymbol{p}_V' = -\boldsymbol{p}_r$ by Eq. (34), the choice of $\boldsymbol{p}_{r_0}^{(0)} = \boldsymbol{0}$ implies a reasonable expectation that $\boldsymbol{p}_V$ does not change rapidly from $\boldsymbol{p}_{V_0}^{(0)}$, at least initially.

The time of flight t_f may be desired to be bounded by an upper and lower bound. In our implementation for any unknown u that is bounded by given bounds $u_{min} \le u \le u_{max}$, a transformation is used

$$u = \frac{u_{max} + u_{min}}{2} + \frac{u_{max} - u_{min}}{2} \sin\eta \tag{52}$$

and the algorithm works to find the unconstrained variable η instead.

D. On-Board Computational Viability

The computation required to solve the root-finding problem in the preceding subsection is well within the capability of modern flight computers. As a comparison, UPG runs at least an order of magnitude faster than the Fully Numerical Predictor-corrector Entry Guidance (FNPEG) algorithm reported in Refs. [28, 29]. Benchmark evaluations of the computation requirements of FNPEG concluded that the computation was comparable to the current primary entry guidance algorithm for the Orion spacecraft. [29] In a different application, FNPEG was successfully implemented in flight software in a flight processor and demonstrated in real-time executions. [30] The fact that UPG is considerably faster still than FNPEG provides the confidence of on-board computational viability of the algorithm.

V. Optimal Thrust Profile and Burn Times

A. Structure of Fuel-Optimal Thrust Magnitude Profile

In a one-dimensional fuel-optimal descent problem it is known that the optimal thrust magnitude is piecewise constant, either at the upper or lower bound, and the thrust has at most one switch between the two bounds. [31] For a class of two-dimensional (2-D) optimal rocket flight problems that include the 2-D fuel-optimal powered descent problem in a constant gravity field, the thrust magnitude is also bang-bang type, but can have up to two switches. [32] The questions to which we seek answers are (1) for the *three-dimensional* fuel-optimal problems as posed in Section II, is the optimal thrust magnitude profile still bang-bang? (2) what is the maximum possible number of switches in the thrust magnitude profile, if the answer to (1) is positive? The answers will help greatly simplify the design of the fuel-optimal guidance algorithm. The answers are summarized in the following Proposition.

Proposition

In a constant gravity field, the three-dimensional optimal powered descent problems formulated in Section II have a piecewise constant thrust magnitude profile, either at T_{max} or T_{min}. No other intermediate value (constant or time varying) over a *finite* time period is optimal. Moreover, there are at most two switches in the optimal thrust magnitude between the upper and lower bounds of the thrust, thus the problems have at most 3 subarcs of constant thrust magnitudes (at the upper or lower bound).

Proof: The details of the proof are provided in the Appendix.

Based on the conclusion in the Proposition, in UPG the default thrust magnitude structure is as shown in Fig. 1. The switch times t_1 and t_2 and the final time t_f are all to be found as part of the optimal solution. Note that by allowing the possibilities of $t_1 = 0$, $t_2 = t_1$, and $t_f = t_2$, this thrust structure may lead to special-case sequences of T_{min}-T_{max}, T_{max}, T_{min}, and T_{max}-T_{min}. The only possibility among all three-arc thrust structures not included in a variation of the profile in Fig. 1 is the sequence of T_{min}-T_{max}-T_{min}. For a powered descent problem where the final velocity is constrained, it can be argued that the last thrust arc must be at T_{max} if T_{min} is sufficiently small. For example, if $T_{min} = 0$, the powered descent trajectory cannot possibly end with $T = T_{min}$ (free

fall) because the final velocity constraint will not be met with a zero (or small) thrust acceleration. Indeed, existing numerical results on fuel-optimal powered descent trajectories in the literature [10, 12, 13, 16–18] all confirm this conclusion. Therefore, the generic 3-arc thrust structure in Fig. 1 captures all the possible cases in fuel-optimal powered descent.

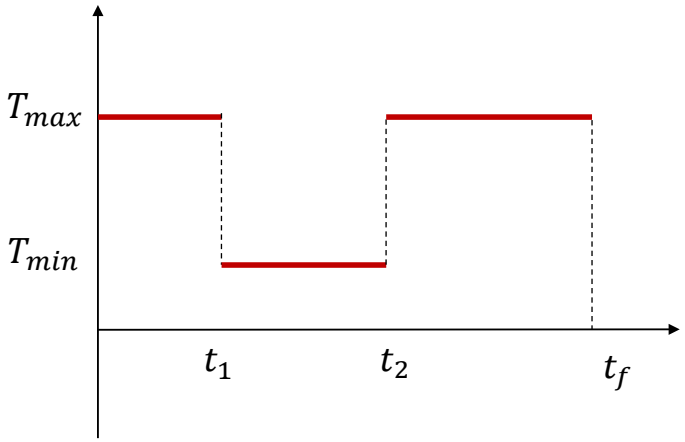

Figure 1. Default thrust magnitude profile

B. Optimal Burn Times

The determination of the optimal switching times t_1 and t_2 in Fig. 1 in principle may be found by computing the switching function (see Appendix). But this is an unreliable way, because slightly less perfect initial guesses could dramatically alter the resulting thrust magnitude profile, making convergence difficult to achieve. The outer-loop minimization method described below is much more robust and efficient.

For specified switching times t_1 and t_2, the basic algorithm outlined in Section IV will find the corresponding optimal solution including the optimal values for t_f and the performance index. For now let us assume that t_1 is fixed. Therefore the optimal performance index is a univariante function of t_2: for a given value of t_2, the optimal performance index has a corresponding value. Denote the optimal performance index by $J^*(t_2)$ corresponding to the given t_2 to signify its dependence on t_2. Evaluating $J^*(t_2)$ is fast because the basic algorithm finds the solution very rapidly. An outer-loop is built around the basic algorithm to update the value of t_2 and further reduce the value

of $J^*(t_2)$ over t_2. This outer-loop is exited once $J^*(t_2)$ reaches its minimum with respect to t_2. The optimal t_2 is then found. Brent's method, [33] a well-recognized univariate minimization method that combines the strengths of bi-section and inverse-quadratic interpolation approaches, is used in this outer loop to find the optimal t_2. For on-board applications, this outer-loop is run only once. It is found that continuing to update the optimal t_2 in subsequent guidance cycles produces negligible benefits in propellant consumption.

In principle the same logic can be used to regard the optimal performance index as a function both t_1 and t_2, and find the optimal t_1 and t_2 in an outer-loop of bi-variante minimization. We have implemented a version of the algorithm to do just this. However, for the powered descent problem, it was discovered that the optimal propellant usage is very insensitive to the variations of t_1 (at least if t_1 is in a reasonable range), as long as t_2 and t_f are optimized. To demonstrate this finding, a human Mars mission scenario with a vehicle of 58000 kg at entry is used. More vehicle and mission data are given in Section VIII later. Each of the 3 curves in Fig. 2 corresponds to a particular initial condition for the powered descent phase, signified by the different values of the initial altitude h_0. Other states such as velocity and position corresponding to each h_0 are all defined by the entry trajectory prior to the powered descent phase. Starting at the condition defined by h_0, a sequence of values of the burn time t_1 of the first full-throttle arc is taken. For each of these t_1's, the powered descent algorithm plus the outer loop described in the preceding paragraph is used to find the optimal descent trajectory (including the optimal t_2) in closed-loop simulation, and the landing mass is recorded.

It can be seen from Fig. 2 that as long as t_1 is not too long (e.g., less than 20 seconds), the landing mass (or equivalently propellant usage) under the guidance algorithm has little difference for different values of t_1. Indeed, the difference between the highest landing mass at the optimal t_1 and the landing mass at a non-optimal t_1 is less than 100 kg for a vehicle of more than 47,000 kg in landing mass (again for $t_1 \leq 15 \sim 20$ sec). In a way, the optimization of $t_2 - t_1$ and $t_f - t_2$ for each given t_1 contributes to the insensitivity of the propellant usage with respect to t_1. Therefore optimizing t_1 brings little additional advantage when $t_2 - t_1$ and $t_f - t_2$ are optimized. In the rest of this paper, the powered descent guidance algorithm is assigned a fixed t_1 ($t_1 = 10$ sec for the

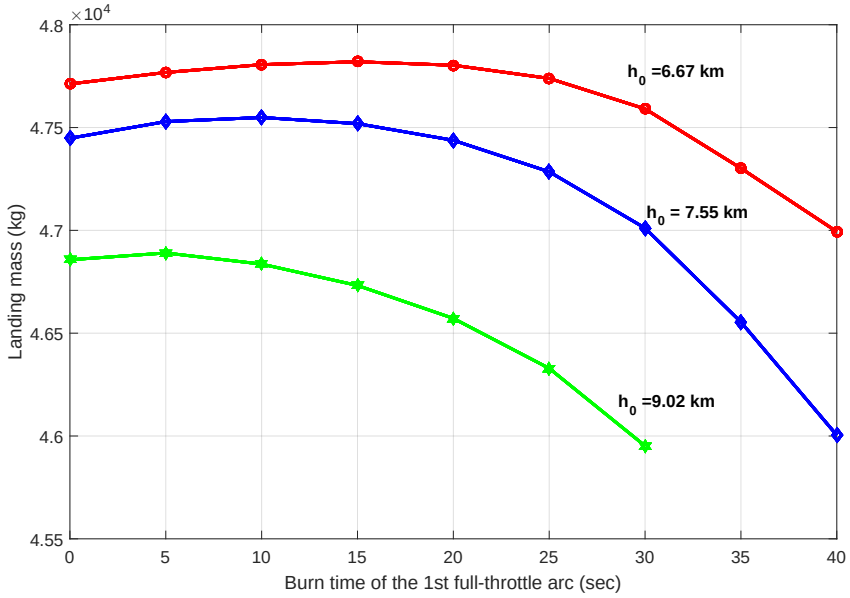

Figure 2. The effects of t_1, the burn time of the first full-throttle arc

numerical results in this paper. This value may be adjusted for a particular vehicle).

In a sharp contrast to the insensitivity of the propellant usage with respect to t_1, an optimal throttle-back phase in the middle of the 3-arc trajectory (i. e., the optimization of t_2) has a significant impact on propellant usage. Figure 3 shows the landing masses of the same vehicle when the powered descent phase starts at several different altitudes along an entry trajectory. The (blue) solid curve is for the cases under UPG with the three-arc optimal thrust profile as in Fig. 1. The cases on the dashed curve use full thrust all the way (no throttle-back arc) in the same missions, but otherwise the burn time and thrust direction are optimal, all determined by the same basic algorithm in Section IV. When the retro-engine is turned on at the lowest altitude tested ($h_0 = 5.7$ km), the two guidance strategies yield the same landing mass. This is because in this case the optimal burn time of the throttle-back phase is found to be zero ($t_2 = t_1$), and the solutions are the same as the full-throttle trajectory. This is about the last condition where a powered descent trajectory satisfying the specified position and velocity condition at the landing site still exists. As the engine ignition altitude becomes higher, the distance at the beginning of powered descent is also further away from the landing site, and the landing mass advantage by the guidance strategy with the optimal 3-thrust-arc structure grows rapidly. The difference reaches about 3600 kg when $h_0 = 9.02$

km. Thus, it is essential for a propellant-optimal powered descent guidance algorithm to use the 3-arc bang-bang thrust structure. Furthermore, it may be observed on the basis of Fig. 3 that *the optimal 3-thrust-arc solution in powered descent significantly reduces the sensitivity of propellant usage with respect to the initial condition of the powered descent phase.*

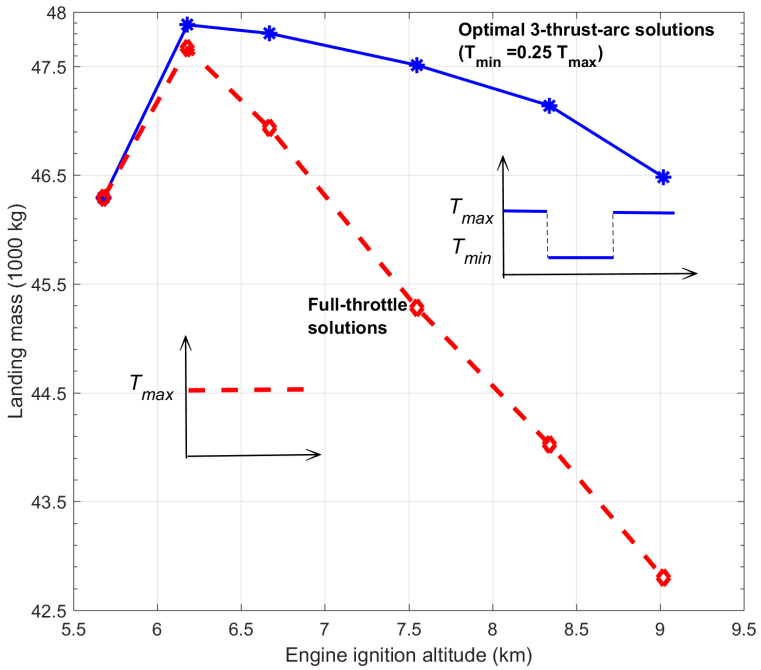

Figure 3. Comparison of the landing mass performance between the optimal 3-thrust-arc solutions and full-throttle solutions with different powered descent initiation conditions

VI. Adaptive Powered Descent Initiation

While the issue of when is best to initiate the powered descent phase is largely omitted in the guidance literature, it is rather consequential. A less favorable powered descent initiation (DPI) condition could result in a large divert requirement thus push the powered descent trajectory close to the capability limit of the vehicle. A poor choice could render soft landing at the designated site impossible. In this section we attempt to answer two pertinent questions:

(1) What is a "good" DPI condition?

(2) How to determine such a condition adaptively *on-board* without requiring complex logic?

For the discussion in this section, we will assume that the vehicle is on a lifting entry or ballistic trajectory flying toward the landing site before the powered descent phase begins. We will refer only to entry trajectory hereafter to avoid repeating the reference to "ballistic trajectory" simultaneously, while keeping in mind that everything discussed in this section applies to ballistic pre-powered-descent flight (as in a lunar landing).

Under the preceding assumption, the initiation condition of the powered descent phase will be a point on the entry trajectory. We will call a point on this entry trajectory a *feasible* point if by starting the powered descent phase at the point, the vehicle can still land softly at the designated site within the maximum propellant consumption the vehicle allows. Obviously the collection of all feasible points forms a continuous segment on the entry trajectory somewhere before the landing site. A normal entry trajectory is such that the last feasible point has the lowest altitude and velocity, and the shortest distance to the landing site, among all feasible points. Powered descent trajectories starting after this critical condition would either require an unattainable divert or not have sufficient time (or altitude) to take out the excess velocity before hitting the ground.

For question (1), we submit that propellant consumption alone is not a sufficient criterion to define a good DPI condition. Recall Fig. 3. The two curves in Fig. 3 unmistakably show that if the initial condition of the powered descent phase can be selected, the overall least propellant usage (or the overall largest landing mass) is achieved by the fuel-optimal guidance at a condition around the altitude of 6.2 km, close to the last feasible point on the entry trajectory (which is at about an altitude of 5.7 km for the vehicle and mission in Fig. 3). But choosing the PDI at $h_0 = 6.2$ km leaves little operational margin for the powered descent trajectory. Even small dispersions could push the PDI condition into the side of steep drop in landing mass seen in Fig. 3. Moderate dispersions could render the PDI condition infeasible. Therefore a good DPI condition should be one that strikes a balance between propellant usage and robustness of the descent trajectory.

Toward this end, the soft-landing mode of the guidance algorithm proves to be enabling. Recall that the soft-landing trajectory satisfies the final velocity constraints and altitude constraint, but the landing location is unconstrained. The conditions along the entry trajectory are such that, when starting at a point on this trajectory, the soft-landing descent trajectory will be flying in the general

direction of the landing site. Once the vehicle gets below a threshold velocity along the entry trajectory, the soft-landing mode of the powered descent guidance algorithm is called periodically (e. g., at 0.1 HZ). The solution will provide the predicted landing location if the powered descent were to start now and a soft-landing trajectory were flown. Initially the downrange to the landing site at the predicted landing location will be shorter than the actual range to the landing site (an undershoot). As the vehicle gets closer to the landing site, the difference between the two ranges will be smaller and smaller. Eventually the predicted downrange to the landing site at the predicted landing location will be an overshoot. Figure 4 illustrates this idea with the vehicle and mission data to be presented in Section VIII. The last predicted soft-landing trajectory in Fig. 4 is where the overshoot first takes place. At this moment, the powered descent phase should begin. The powered descent trajectory will then be guided by the pinpoint-landing mode of the guidance algorithm to ensure the satisfaction of the final position and velocity (vectors) constraints. The maneuvers required by the pinpoint-landing mode should be similar to those along the soft-landing trajectory and the propellant usage should be just slightly higher than that by the soft-landing trajectory, because of the closeness of the two trajectories when both start at this particular point on the entry trajectory. In other words, the pinpoint-landing trajectory will have a good propellant performance (cf. Property 4 in Section III) while requiring no aggressive divert maneuvers. The working of entry and powered descent guidance and the transition between the two phases defined by the PDI are summarized as follows

1. Starting at the entry interface, entry guidance system guides the vehicle

2. Once the planet-relative velocity is below a prescribed threshold V_s, begin to periodically call the powered descent guidance algorithm in the soft-landing mode to predict the touchdown downrange to the landing site. If the predicted downrange is an undershoot, continue with entry guidance.

3. As soon as the predicted touchdown is an overshoot, initiate the powered descent phase

4. Powered descent guidance in the pinpoint-landing mode takes over and guides the vehicle to land at the landing site.

Figure 5 shows the flow chart that depicts this sequence of guidance phases and the determination of PDI just outlined.

Step 3 in the above logic may be modified slightly to check the condition whether "predicted touchdown range ≥ actual ground range +Δ", where $\Delta \geq 0$ is a specified small margin (e. g., 1 to 3 km). A $\Delta > 0$ means the allowance of a moderate overshoot of the soft-landing trajectory, and can typically lead to some additional propellant saving as the PDI will occur at a lower velocity.

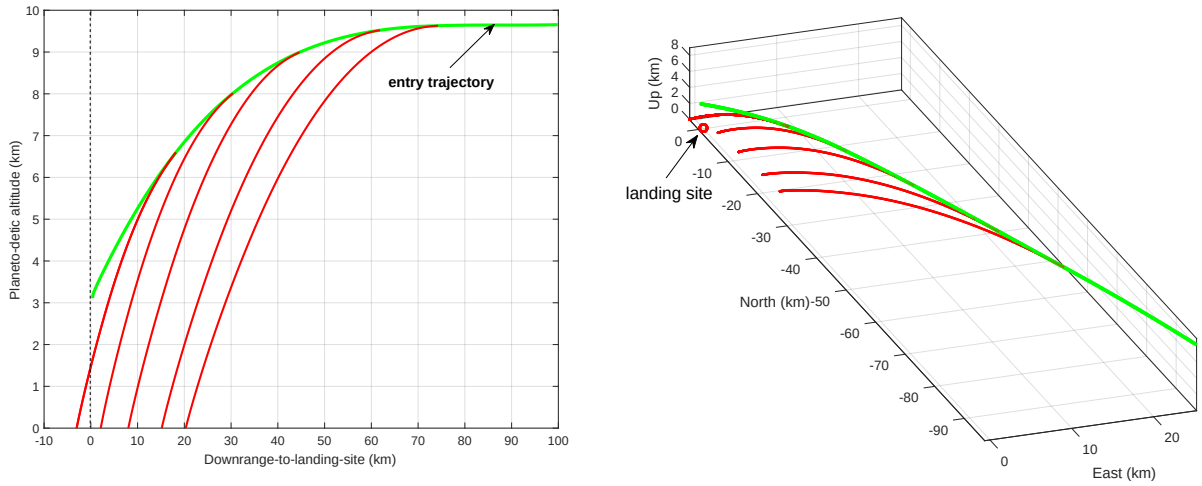

a) Soft-landing downranges **b) 3-D soft-landing trajectories**

Figure 4. Soft-landing trajectories starting at different points along an entry trajectory

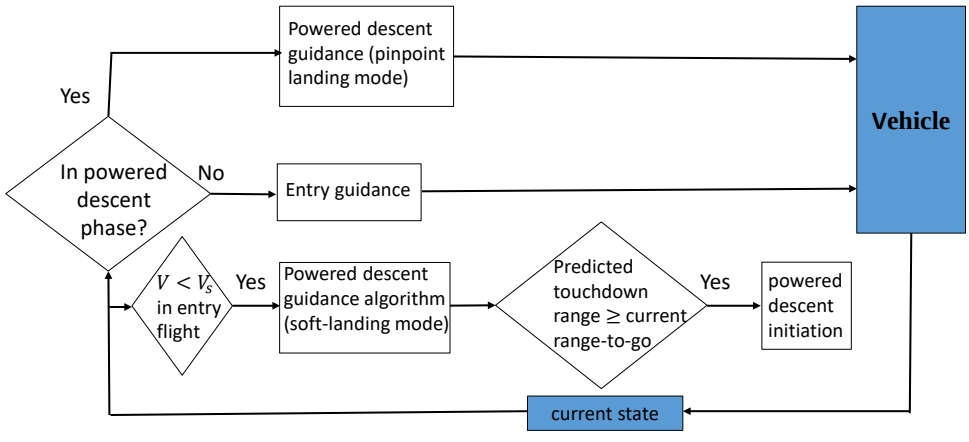

Figure 5. Integrated guidance functions from entry to powered descent with adaptive powered descent initiation

VII. Terminal Descent Phase Guidance

Just like in Apollo lunar descent, a terminal descent phase may be added before touchdown that will allow further shaping of the trajectory so as to ensure the correct attitude of the vehicle (through the appropriate direction of the thrust vector) during the final descent and at touchdown. If a terminal descent phase is used, the targeting condition for the pinpoint-landing mode in UPG can be set, for instance, at a specified height right above the landing site with a given descent rate. Other targeting conditions similar to that in the approach phase in the Apollo descent guidance [2] may be used. The handover to the terminal descent guidance should occur, however, at a specified (nonzero) ground range to the landing site. This prevents the terminal descent trajectory from overshooting the landing site. The terminal descent guidance will take the vehicle from the actual state at the termination of UPG to the landing site with soft touchdown. The following Apollo lunar descent guidance law in Refs. [1, 2] works well in this short final phase of descent

$$\boldsymbol{a}_T = -\frac{6}{t_{go}}\left[\boldsymbol{V}^* - \boldsymbol{V}(t)\right] + \frac{12}{t_{go}^2}\left[\boldsymbol{r}^* - \boldsymbol{r}(t) - \boldsymbol{V}(t)t_{go}\right] + \boldsymbol{a}_f^* \tag{53}$$

where $\boldsymbol{a}_T = \boldsymbol{T}(t)/m(t)$, $t_{go} = t_f - t$, and $\boldsymbol{a}_f^*$ is a specified final thrust acceleration vector. This guidance law comes from a desired $\boldsymbol{r}(t)$ profile of a quartic polynomial in time that meets the initial state condition and specified terminal conditions in position, velocity, and thrust acceleration. Note that the guidance law in Eq. (53) defines both the thrust magnitude and direction. Since the time-to-go t_{go} approaches zero, the use of this guidance law is stopped shortly before touchdown to avoid singularity. A constant $\boldsymbol{a}_T$ command from the last calculation suffices in this short period.

The guidance law in Eq. (53) is not propellant-optimal. But if t_{go} is appropriately chosen (that is reasonably short), the propellant usage will be close to optimum. For the terminal descent phase, a good estimate of t_{go} may be obtained from the gravity-turn solutions first presented in Ref. [34]. In this approach the required constant thrust-acceleration value a_T in the gravity turn is calculated so that the velocity will be zero just when the altitude is zero. This value of a_T is determined by

solving the following quadratic equation in a_T (cf. Eq. (31) in Ref. [34]):

$$a_T^2 + \left(\frac{V_0^2 \sin\gamma_0}{2h_0}\right) a_T - \left[\frac{V_0^2 g(1+\sin^2\gamma_0)}{4h_0} + g^2\right] = 0 \tag{54}$$

where γ_0, h_0 and V_0 are the initial flight path, height, and velocity for the terminal descent. With a $\gamma_0 \leq 0$, this equation has just one positive real root, thus there is no ambiguity in deciding which root to use. Or Eq. (54) may be use to determine the initial height h_0 of the terminal descent phase when a_T is specified (say, $a_T = \|\boldsymbol{a}_f^*\|$). Once a_T is defined, the time it takes along the gravity turn trajectory with this a_T to hit the ground can be found (cf. Eq. (33) in Ref. [34]). An appropriately scaled-up value may be used as an estimate for the initial time-to-go in the guidance law in Eq. (53):

$$t_{go} = k\frac{V_0}{2}\left(\frac{1+\sin\gamma_0}{a_T+g} + \frac{1-\sin\gamma_0}{a_T-g}\right) \tag{55}$$

where $k > 1.0$ (e. g., $k = 1.2$) is a scaling factor that is judiciously determined to account for the fact that the trajectory under Apollo guidance law Eq. (53) is not exactly a gravity turn. The subsequent values of t_{go} are determined by this initial value minus the time elapsed.

VIII. Closed-Loop Simulations

The UPG algorithm is implemented in a three-degree-of-freedom simulation environment for verification and demonstration. More extensive testing and evaluations with high-fidelity Monte Carlo simulations will be reported at a later time. The mission scenario used here is a humane Mars entry, descent and landing (EDL) mission. The vehicle has an aeroshell configuration that is called the mid lift-to-drag ratio Mars rigid vehicle (MRV). [35] Figure 6 shows the concept of operations for the MRV in Mars EDL missions. More details on the concept and vehicle design are described in Ref. [35]. At the entry interface the MRV has a mass of 58000 kg, with a L/D ratio of 0.58 and ballistic coefficient of 397 kg/m^2. The MRV is fitted with a supersonic retro-propulsion (SRP) system with 8 engines (4 mounted on each side of the MRV). Each engine produces at full throttle a thrust of 100000 N, and has a specific impulse of 360 seconds. It is assumed that the lowest throttle allowed is 25%.

At the entry interface the MRV has an altitude of 129.18 km and relative velocity of 4694 m/s. The downrange to the landing site is 710 nautical miles (nm). The entry flight is from south to north and is guided by the Fully Numerical Predictor-corrector Entry Guidance (FNPEG) algorithm. [28, 29]. In closed-loop simulations FNPEG is called at 1 Hz. The bank angle rate and acceleration are limited by 15 deg/s and 5 deg/s^2, respectively. After PDI the powered descent guidance algorithm UPG is called at a 5 Hz frequency. For the MRV, the SRP engine thrust is assumed to be aligned with the body-normal axis (see Fig. 6). The direction of the thrust vector therefore defines the body frame. In powered descent simulations, the vehicle body attitude Euler angles are subject to a rate limit of 15 deg/s.

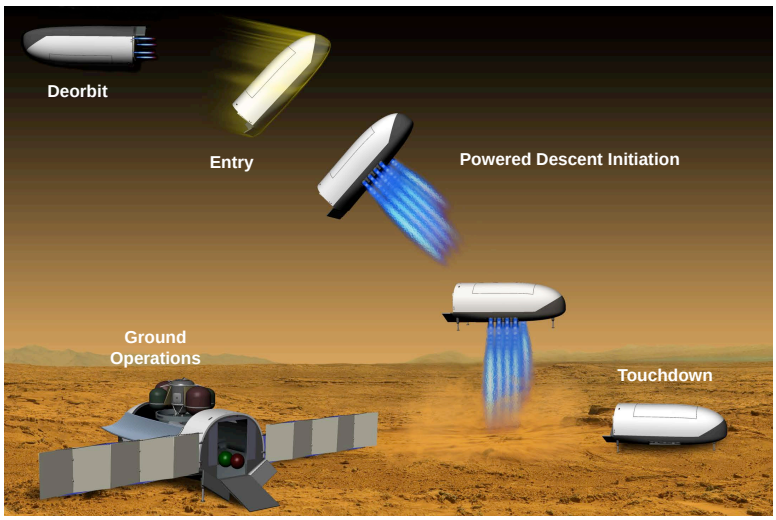

Figure 6. Concept of operations for the mid L/D rigid vehicle in Mars entry, descent and landing (courtesy of Ref. [35])

A. Powered Descent from Different Conditions

As the first demonstration of UPG, 6 different points along the entry trajectory are picked to be the powered descent initiation conditions. The corresponding Mars-relative velocity, altitude, and ground range to the landing site for the 6 cases are summarized in Table 1. The targeting condition for the UPG is zero altitude at the landing site with a descent rate of 1.0 m/s. No terminal descent phase is used.

The six optimal descent trajectories guided by UPG are shown in Fig. 7. The thrust acceleration

Table 1. Powered descent initiation conditions of the test cases

	Case 1	Case 2	Case 3	Case 4	Case 5	Case 6
velocity V_0 (m/s)	562.1	573.6	585.2	608.8	633.2	658.6
altitude h_0 (m)	5,469.6	5,996.3	6,477.4	7,365.7	8,152.1	8,830.6
ground range s_0 (m)	10,099.8	12,542.1	15,040.6	20,207.1	25,602.3	31,230.7

and engine throttle profiles are illustrated in Fig. 8. The optimal throttle-back phase at $T_{min} = 0.25T_{max}$ has a duration ranging from zero sec in Case 1 to 45.3 sec in Case 6. In general, the further away the PDI condition is from the landing site, the longer the throttle-back phase lasts. This is the most influential factor in the propellant-optimal powered descent trajectory responsible for saving fuel. The landing mass comparison is very similar to what the solid curve in Fig. 3 shows. The total flight times among the 6 cases range from 52 seconds in Case 1 to 84 seconds in Case 6. Case 1 is about to be the latest point along this particular entry trajectory from where a feasible powered descent trajectory still exists.

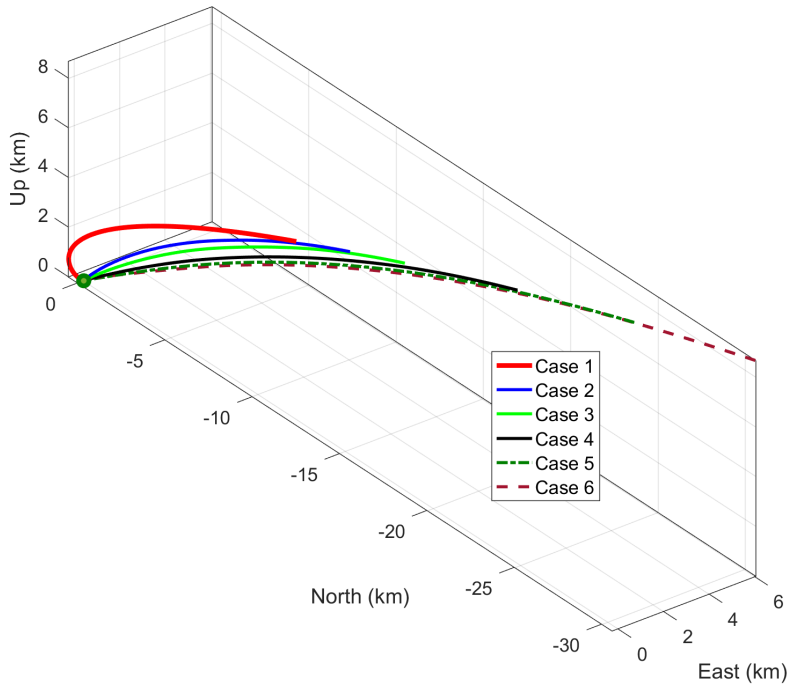

Figure 7. Powered descent trajectories for the 6 cases in Table 1

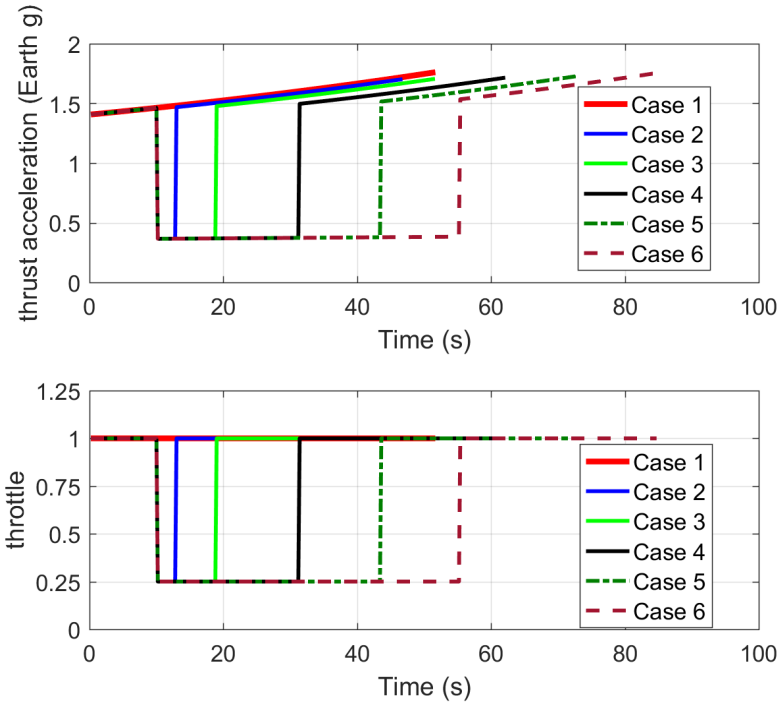

Figure 8. Thrust acceleration magnitude and throttle profiles for the 6 cases in Table 1

B. Powered Descent Initiation

In this section the adaptive PDI logic developed in Section VI is demonstrated. As soon as the Mars-relative velocity is below the threshold value of $V_s = 700$ m/s along the FNPEG guided entry trajectory, the PDI condition check depicted in Fig. 5 is performed periodically at 1 Hz rate. The PDI condition is determined this way to be at a velocity of 646.4 m/s (Mach 2.86) and a planeto-detic altitude of 7189.6 m, with a ground range of 23666.8 m to the landing site. Figure 9 shows the combined trajectory in altitude versus relative velocity. The thrust acceleration magnitude and throttle for the powered descent phase are plotted in Fig. 10. The corners in the velocity profile during powered descent in Fig. 9 are caused by the switches in the throttle in Fig. 10.

Next, to demonstrate how this PDI logic works in more cases, the entry flight path angle of the mission is dispersed uniformly around its nominal value in the range of $[-0.3,\ 0.1]$ degree. Initial flight path angle is the most influential parameter to cause changes in the entry trajectory. In any of the dispersed case the corresponding PDI condition should be found automatically by the adaptive scheme that lead to successful powered descent and landing. Figure 11 shows several dispersed

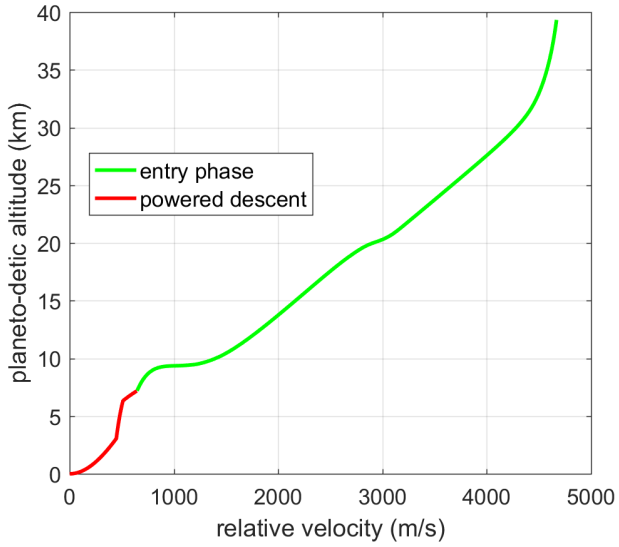

Figure 9. Trajectory in entry and powered descent phases

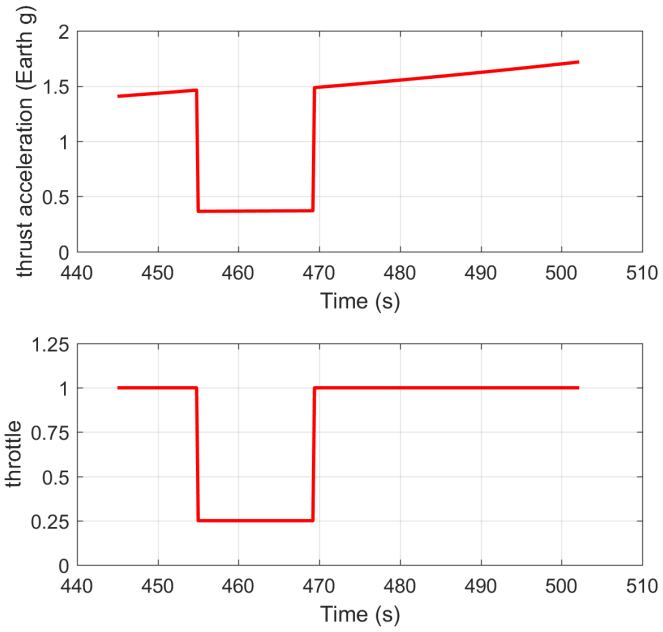

Figure 10. Thrust acceleration and engine throttle in powered descent

trajectories in transition from entry to powered descent. Indeed, the spread of the downrange and altitude at PDI is quite substantial. The same PDI points are also plotted in altitude-vs-velocity in Fig. 12 where the different values of the PDI velocity can be clearly seen. Figures 11 and 12 help illustrate that in the presence of large trajectory dispersions, a prescribed PDI based on a simple state condition-triggered event is not likely to work well for all cases.

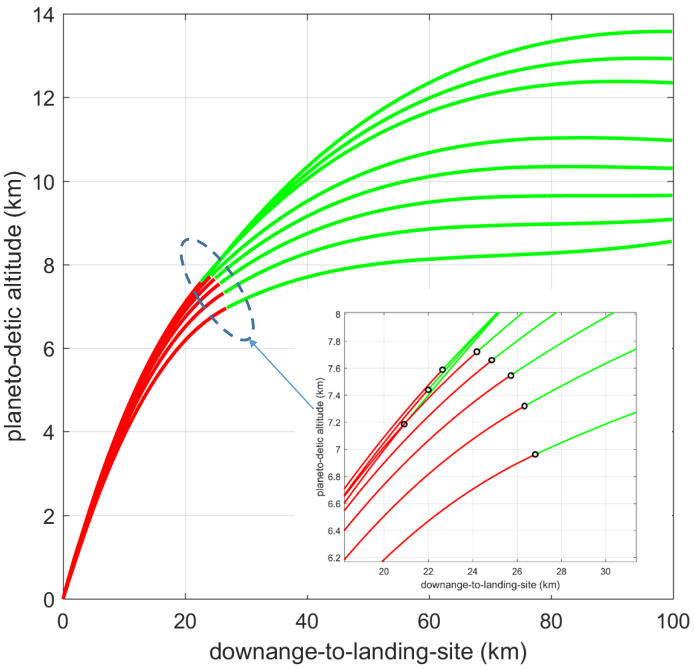

Figure 11. Dispersed entry trajectories and corresponding powered descent trajectories; the adaptively determined powered descent initiation points are shown in the zoom-in insert

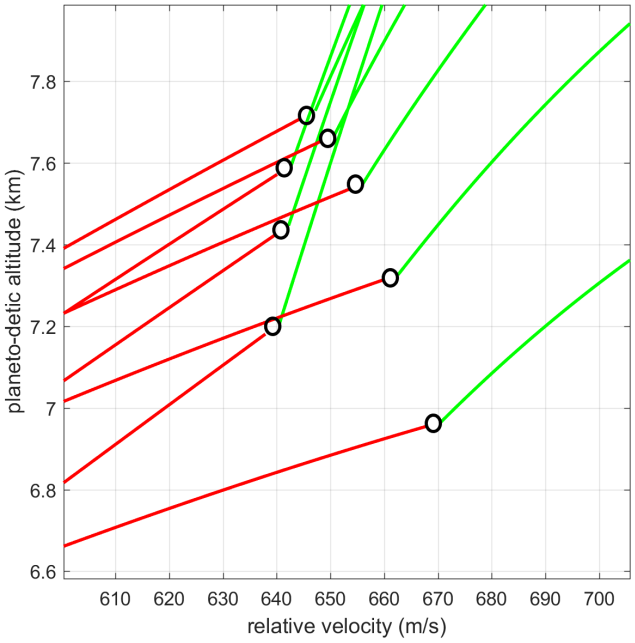

Figure 12. Adaptively determined powered descent initiation points on the dispersed trajectories in the altitude-velocity space

C. Terminal Descent Phase

In this section a terminal descent phase as described in Section VII is added in the powered descent flight. Case 3 in Table 1 is used for illustration. To accommodate a terminal descent phase, the targeting condition for UPG is changed to an altitude of 100 m with a descent rate of 8 m/s right above the landing site. The handover from UPG to the terminal phase guidance law in Eq. (53) takes place at a ground range of 200 m to the landing site. The final condition for the terminal phase guidance has the same final condition as in the preceding two subsections, at zero altitude at the landing site with a descent rate of 1 m/s. In addition, the final thrust acceleration vector $\boldsymbol{a}_f^*$ is vertically up at the landing site, with a magnitude of 6.42 m/s^2 (2 Mars gs).

The throttle along the powered descent trajectory is given in Fig. 13. The variable throttle during the terminal descent phase can be clearly seen, where the terminal descent phase lasts 10.8 seconds. The 3-arc bang-bang throttle by UPG (for the same final condition) without the terminal phase is also plotted in Fig. 13 for comparison. The propellant usage by the powered descent trajectory with the terminal descent phase is 10,435 kg, whereas the trajectory without the terminal descent phase consumes 10,197 kg of propellant. This propellant penalty of 238 kg is partially due to the non-fuel-optimal nature of the Apollo guidance law (and partially due to the additional constraint on final thrust vector), but this is in the context of an initial vehicle mass of 58,000 kg.

A main benefit of the terminal descent phase is a more desirable final attitude of the vehicle at landing. Figure 14 shows the body pitch and yaw angles with respect to the North-East-Down frame at the landing site, in a 3-2-1 rotation sequence. Indeed, with the terminal descent phase, the final pitch angle of the vehicle is zero, indicating that the vehicle lands with the correct attitude. Without the terminal descent phase, the pitch angle of the vehicle is still at 40 degrees at touchdown. The geometric shapes of the descent trajectories in the last moments with and without the terminal descent phase are compared in Fig. 15. With the terminal descent phase, the trajectory descends onto the landing site along a nearly vertical path, whereas the trajectory without the terminal descent phase is more shallow, indicating a larger horizontal velocity near the end.

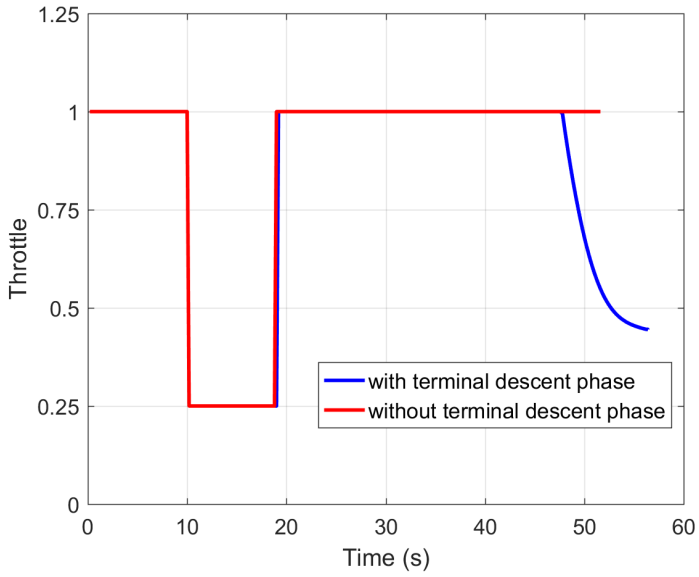

Figure 13. Throttle profiles with and without a terminal descent phase

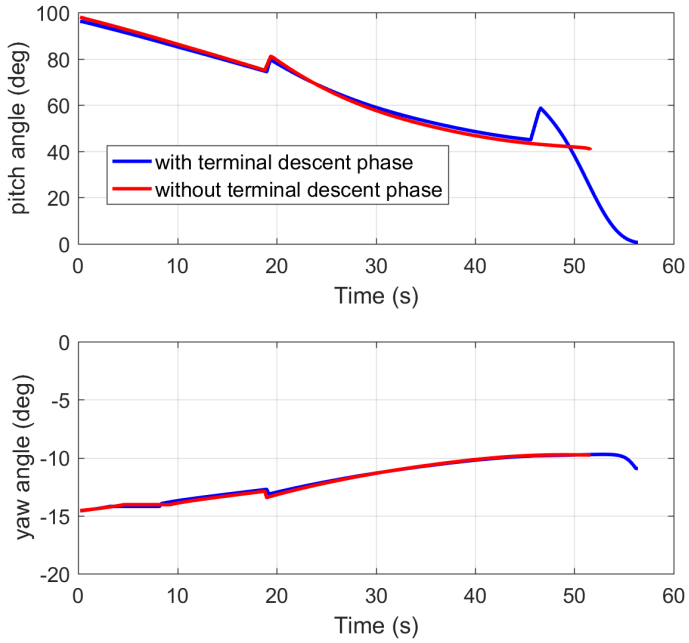

Figure 14. Body attitude Euler angles with and without a terminal descent phase

IX. Conclusions

In this paper a propellant-optimal rocket powered descent guidance algorithm is developed. The algorithm is capable of solving a family of free-time propellant-optimal descent problems. Each

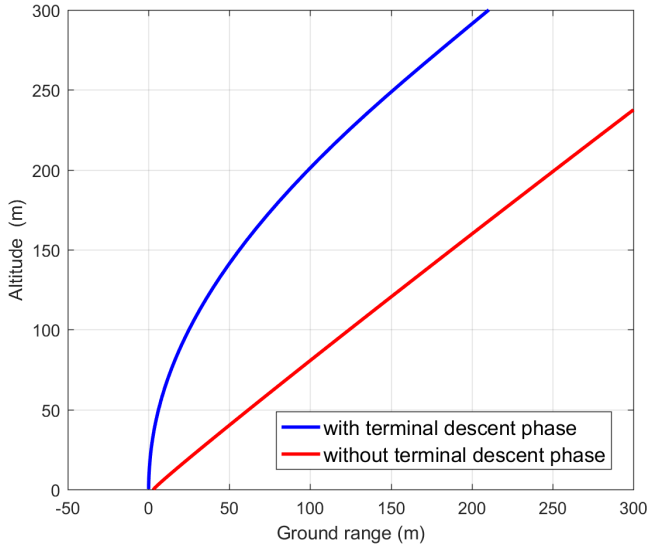

Figure 15. The last part of the powered descent trajectories with and without a terminal descent phase

of the problems serves a particular objective potentially useful in powered descent. An analysis based on the optimal control theory establishes that under the assumption of constant gravity field, these problems will have an optimal thrust magnitude profile that is either on the upper bound or lower bound, and no singular thrust arc can be optimal. Moreover, the number of switches between the thrust magnitude bounds is no more than 2. Taking advantage of these theoretical findings, a fast and robust guidance algorithm based on the indirect method, dubbed Universal Powered Guidance (UPG), is developed to reliably and efficiently solve the problems. Another unique capability of UPG is adaptive determination of the initiation point of the powered descent phase that renders a small divert requirement during the descent. When necessary, Apollo descent guidance may be used for a terminal descent phase following UPG guidance to shape the trajectory for a vertical landing. The functionalities and capabilities of UPG are clearly demonstrated by closed-loop numerical simulations for a human Mars mission.

Acknowledgments

This research has been supported in part by NASA Cooperative Agreement NNX16AL35A. Technical discussions with Christopher Cerimele, Ronald Sostaric, and Gavin Mendeck of NASA Johnson Space Center were influential in shaping this work.

Appendix: Structure of Optimal Thrust Magnitude Profile

In this appendix we prove that for the optimal powered descent problems in Section II in a constant gravity field, the optimal thrust magnitude profile must be on the upper or lower bound, and no intermediate value in a finite interval is optimal. Furthermore, the optimal thrust magnitude switches between the upper and lower bounds at most twice, producing at most three subarcs in the complete trajectory. The proof is actually done in a more general context for a class of three-dimensional (3-D) optimal rocket flight problems that include the propellant-optimal powered descent problems in Section II.

The class of problems is defined first. The equations of 3-D motion are the same as in Eqs. (1)–(3), with $\boldsymbol{g}$ now regarded as a *constant* vector. The controls are still the unit thrust vector $\mathbf{1}_T$ and thrust magnitude T, subject to the constraints in Eqs. (5) and (6). The initial and final states are constrained appropriately, but otherwise no particular forms are required:

$$\boldsymbol{q}[\boldsymbol{r}(t_0), \boldsymbol{V}(t_0), m(t_0)] = \mathbf{0} \tag{56}$$

$$\boldsymbol{s}[\boldsymbol{r}(t_f), \boldsymbol{V}(t_f), m(t_f)] = \mathbf{0} \tag{57}$$

where the final time t_f is free. The performance index considered in this class of problems is of Mayer type:

$$J = \phi[\boldsymbol{r}(t_f), \boldsymbol{V}(t_f), m(t_f)] \tag{58}$$

Note that boundary constraints and performance index are broader than but include the powered descent problem. For instance for a specified initial mass and $\phi = -m(t_f)$, the performance index in Eq. (58) is the same as the integral in Eq. (11). For this class of problems the Hamiltonian is

$$H = \boldsymbol{p}_r^T \boldsymbol{V} + \boldsymbol{p}_V^T \left(\boldsymbol{g} + \frac{T}{m} \mathbf{1}_T \right) - p_m \frac{T}{v_{ex}} = \boldsymbol{p}_r^T \boldsymbol{V} + \boldsymbol{p}_V^T \boldsymbol{g} + T \left(\frac{1}{m} \boldsymbol{p}_V^T \mathbf{1}_T - \frac{p_m}{v_{ex}} \right) \tag{59}$$

The costate equations are

$$\dot{\boldsymbol{p}}_r = -\frac{\partial H}{\partial \boldsymbol{r}} = \mathbf{0} \tag{60}$$

$$\dot{\boldsymbol{p}}_V = -\frac{\partial H}{\partial \boldsymbol{V}} = -\boldsymbol{p}_r \tag{61}$$

$$\dot{p}_m = -\frac{\partial H}{\partial m} = \frac{T}{m^2}\boldsymbol{p}_V^T \mathbf{1}_T \tag{62}$$

The first two costate equations have the solution of

$$\boldsymbol{p}_r = -\boldsymbol{c}_1, \quad \boldsymbol{p}_V = \boldsymbol{c}_0 + \boldsymbol{c}_1 t \tag{63}$$

where $\boldsymbol{c}_0$ and $\boldsymbol{c}_1$ are constant vectors. The unit control vector $\mathbf{1}_T$ maximizing H is given by

$$\mathbf{1}_T = \frac{1}{\|\boldsymbol{p}_V\|}\boldsymbol{p}_V \tag{64}$$

Define the switching function

$$S = \frac{1}{m}\boldsymbol{p}_V^T \mathbf{1}_T - \frac{p_m}{v_{ex}} \tag{65}$$

Replacing $\mathbf{1}_T$ by Eq. (64) in Eq. (65)

$$S = \frac{1}{m}\|\boldsymbol{p}_V^T\| - \frac{p_m}{v_{ex}} \tag{66}$$

The optimal thrust magnitude is then determined by maximizing H with respect to T

$$T = \begin{cases} T_{max}, & \text{if } S > 0; \\ T_{min}, & \text{if } S < 0. \end{cases} \tag{67}$$

We will show that the singular case where $S = 0$ and a thrust magnitude profile takes an intermediate (and possibly time-vary) value in a *finite* interval is not optimal in most cases, and certainly not optimal for the powered descent problems in Section II. Differentiate S in Eq. (66) once, and use the costate equations and mass equation to arrive at

$$\dot{S} = -\frac{\boldsymbol{p}_V^T \boldsymbol{p}_r}{m\|\boldsymbol{p}_V\|} \tag{68}$$

With the costate solution in Eq. (63), $\dot{S}$ is further expressed as

$$\dot{S} = \frac{1}{m\|\boldsymbol{c}_0 + \boldsymbol{c}_1 t\|}(a + bt) \tag{69}$$

where $a = \boldsymbol{c}_1^T \boldsymbol{c}_0$ and $b = \boldsymbol{c}_1^T \boldsymbol{c}_1$. If $S = 0$ in a finite interval, it is necessary that $\boldsymbol{c}_1 = \boldsymbol{0}$, thus $a = b = 0$. Therefore $S \equiv 0$ for all $t \in [t_0, t_f]$. In addition, the costate solution for $\boldsymbol{p}_V$ in Eq. (63) reduces to

$$\boldsymbol{p}_V = \boldsymbol{c}_0 \tag{70}$$

Using $\boldsymbol{p}_r = \boldsymbol{c}_1 = \boldsymbol{0}$ and $S \equiv 0$ in the expression of the Hamiltonian H in Eq. (59) results in

$$H = \boldsymbol{p}_V^T \boldsymbol{g} = \boldsymbol{c}_0^T \boldsymbol{g} \tag{71}$$

A transversality condition for the free-time problem under consideration is $H(t_f) = 0$, which in conjunction with the above expression for H gives

$$\boldsymbol{c}_0^T \boldsymbol{g} = 0 \tag{72}$$

One possibility for Eq. (72) is $\boldsymbol{c}_0 = \boldsymbol{0}$. But this solution will lead to $\boldsymbol{p}_V \equiv \boldsymbol{0}$ and $p_m \equiv 0$ (from $S \equiv 0$). The occurrence of a null costate vector contradicts the Maximum Principle [25]. The only other solution for Eq. (72) is that $\boldsymbol{p}_V = \boldsymbol{c}_0$ is perpendicular to the gravitational acceleration vector. From Eq. (64) this implies a constant and horizontal thrust direction, not a possible solution except for rare cases with very special boundary conditions and the matching performance index (see Example (1) in Ref. [32]). A constantly horizontal thrust is certainly not possible for a powered descent problem. Therefore singular thrust arc is not optimal for the powered descent problem.

For the powered descent problems (and other problems with bang-bang thrust magnitude), Eq. (69) implies that $\dot{S}$ changes sign at most once. Since S is continuous, this means that S crosses zero and changes sign at most *twice*. By Eq. (67), the optimal thrust magnitude switches at most twice, rendering at most 3 subarcs where either $T = T_{max}$ or $T = T_{min}$.

Note that this conclusions are not limited to the powered descent problems as defined in Sec-

tion II. The key element that leads to the conclusion on the number of thrust switches is the constant gravity assumption. The underlying physical interpretation is relative short flight range. In a central gravity field, Eq. (68) is still valid, but not Eq. (69). Indeed, if the central gravity field in Eq. (29) is used for longer range flight, and the costate solution in Eq. (36) is used in Eq. (68), $\dot{S}$ can change sign more than twice, resulting in more than 3 subarcs in the trajectory.

Even though similar conclusions are also among the findings in Ref. [32], the case studied in Ref. [32] is limited to two-dimensional motion in a vertical plane. The dimensionality of the problem can cause a difference. In a *one-dimensional* optimal powered descent problem, there is at most just *one* thrust switch. [31] Hence it is necessary and reassuring to rigorously establish the conclusions in this appendix for optimal *three-dimensional* rocket flight. The proof in this appendix is also different (and perhaps easier to follow) than that in Ref. [32], and the language is consistent with the Maximum Principle which is likely more familiar to the reader today.

References

[1] Cherry, G. W., "A General, Explicit, Optimizing Guidance Law for Rocket-Propelled Spaceflight," AIAA Paper 64-638, 1964.
doi:10.2514/6.1964-638.

[2] Klumpp, A. R., "Apollo Lunar Descent Guidance," *Automatica*, Vol. 10, No. 2, 1974, pp. 133–146.
doi:10.1016/0005-1098(74)90019-3.

[3] Goodman, J. L., "Powered Guidance Development for Apollo and the Space Shuttle," AAS Paper 16-093, 2016.

[4] D'Souza, C. S., "An Optimal Guidance Law for Planetary Landing," AIAA Paper 97-3709, 1997.
doi:10.2514/6.1997-3709.

[5] Ross, I. M., "How to Find Minimum-Fuel Controllers," AIAA Paper 2004-5346, 2004.
doi:10.2514/6.2004-5346.

[6] Steinfeldt, B. A., Grant, M. J., Matz, D. M., Braun, R. D., and Barton, G. H., "Guidance, Navigation, and Control Technology System Trades for Mars Pinpoint Landing," *Journal of Spacecraft and Rockets*, Vol. 47, No. 1, 2010, pp. 188–198.
doi:10.2514/1.45779.

[7] Wong, E., Singh, G., and Masciarelli, J., "Guidance and Control Design for Hazard Avoidance and Safe Landing on Mars," *Journal of Spacecraft and Rockets*, Vol. 43, No. 2, 2006, pp. 378–384.
doi:10.2514/1.19220.

[8] Ploen, S., Acikmese, B., and Wolf, A., "A Comparison of Powered Descent Guidance Laws for Mars Pinpoint Landing," AIAA Paper 2006-6676, 2006.
doi:10.2514/6.2006-6676.

[9] Najson, F. and Mease, K., "Computationally Inexpensive Guidance Algorithm for Fuel-Efficient Terminal Descent," *Journal of Guidance, Control, and Dynamics*, Vol. 29, No. 4, 2006, pp. 955–964. doi:10.2514/1.25023.

[10] Topcu, U., Casoliva, J., and Mease, K., "Minimum-Fuel Powered Descent for Mars Pinpoint Landing," *Journal of Spacecraft and Rockets*, Vol. 44, No. 2, 2007, pp. 324–331. doi:10.2514/1.25023.

[11] Sostaric, R. and Rea, J., "Powered Descent Guidance Methods For The Moon and Mars," AIAA Paper 05-6287, 2007. doi:10.2514/6.2005-6287.

[12] Acikmese, B. and Ploen, S. R., "Convex Programming Approach to Powered Descent Guidance for Mars Landing," *Journal of Guidance, Control, and Dynamics*, Vol. 30, No. 5, 2007, pp. 1353–1366. doi:10.2514/1.27553.

[13] Acikmese, B., Scharf, D., Blackmore, L., and Wolf, A., "Enhancements on the Convex Programming Based Powered Descent Guidance Algorithm for Mars Landing," AIAA 2008-6426, Aug. 2008. doi:10.2514/6.2008-6426.

[14] Chomel, C. and Bishop, R., "Analytical Lunar Descent Guidance Algorithm," *Journal of Guidance, Control, and Dynamics*, Vol. 32, No. 3, 2009, pp. 915–926. doi:10.2514/1.37700.

[15] Rea, J. R. and Bishop, R. H., "Analytical Dimensional Reduction of a Fuel Optimal Powered Descent Subproblem," AIAA Paper 2010-8026, 2010. doi:10.2514/6.2010-8026.

[16] Blackmore, L., Acikmese, B., and Scharf, D. P., "Minimum Landing Error Powered Descent Guidance for Mars Landing Using Convex Optimization," *Journal of Guidance, Control, and Dynamics*, Vol. 33, No. 4, 2010, pp. 1161–1171. doi:10.2514/1.47202.

[17] Acikmese, B., Carson, J., and Blackmore, L., "Lossless Convexification of Nonconvex Control Bound and Pointing Constraints of the Soft Landing Optimal Control Problem," *IEEE Transactions on Control Systems Technology*, Vol. 21, No. 6, 2013, pp. 2104–2113. doi:10.1109/TCST.2012.2237346.

[18] Dueri, D., Acikmese, B., Scharf, D., and Harris, M., "Customized Real-Time Interior-Point Methods for Onboard Powered-Descent Guidance," *Journal of Guidance, Control, and Dynamics*, Vol. 40, No. 2, 2017, pp. 197–212. doi:10.2514/1.G001480.

[19] Lu, P., Griffin, B., Dukeman, G., and Chavez, F., "Rapid Optimal Multiburn Ascent Planning and Guidance," *Journal of Guidance, Control, and Dynamics*, Vol. 31, No. 6, 2008, pp. 1656–1664. doi:10.2514/1.36084.

[20] Lu, P. and Pan, B., "Highly Constrained Optimal Launch Ascent Guidance," *Journal of Guidance, Control, and Dynamics*, Vol. 33, No. 2, 2010, pp. 404–414. doi:10.2514/1.45632.

[21] Baldwin, M. and Lu, P., "Optimal Deorbit Guidance," *Journal of Guidance, Control, and Dynamics*, Vol. 35, No. 1, 2012, pp. 93–103. doi:10.2514/1.53937.

[22] Lu, P., Forbes, S., and Baldwin, M., "A Versatile Powered Guidance Algorithm," AIAA Paper 2012-4843, 2012.
doi:10.2514/6.2012-4843.

[23] Luenberger, D. and Ye, Y., *Linear and Nonlinear Programming*, chap. 13, Springer, New York, 4th ed., 2008.

[24] Jezewski, D. J., "An Optimal, Analytic Solution to the Linear-Gravity Constant-Thrust Trajectory Problem," *Journal of Spacecraft and Rockets*, Vol. 8, No. 7, 1971, pp. 793–796.
doi:10.2514/3.30320.

[25] Pontryagin, L. S., Boltyanskii, V. G., Gramkreledze, Q. V., and Mishchenko, E. F., *The Mathematical Theory of Optimal Processes*, Intersciences, New York, 1962, pp. 20–21,311–316.

[26] Pan, P., Chen, Z., Lu, P., and Gao, B., "Reduced Transversality Conditions in Optimal Space Trajectories," *Journal of Guidance, Control, and Dynamics*, Vol. 36, No. 5, 2013, pp. 1289–1300.
doi:10.2514/1.60181.

[27] Powell, M. J. D., *A Fortran Subroutine for Solving Systems of Non-linear Algebraic Equations*, AERE-R, United Kingdom Atomic Energy Authority and H.M. Stationery Office, 1968.

[28] Lu, P., "Entry Guidance: a Unified Method," *Journal of Guidance, Control, and Dynamics*, Vol. 37, No. 3, 2014, pp. 713–728.
doi:10.2514/1.62605.

[29] Lu, P., Brunner, C., Stachowiak, S., Mendeck, G., Tigges, M., and Cerimele, C., "Verification of a Fully Numerical Entry Guidance Algorithm," *Journal of Guidance, Control, and Dynamics*, Vol. 40, No. 2, 2017, pp. 230–247.
doi:10.2514/1.G000327.

[30] Johonson, W., Lu, P., and Stachowiak, S., "Automated Re-entry System Using FNPEG," AIAA Paper 2017-1899, 2017.
doi:10.2514/6.2017-1899.

[31] Meditch, J. J., "On the Problem of Optimal Thrust Programming For a Lunar Soft Landing," *IEEE Transactions on Automatic Control*, Vol. 9, No. 4, 1964, pp. 477 – 484.
doi:10.1109/TAC.1964.1105758.

[32] Leitmann, G., "Class of Variational Problems in Rocket Flight," *Journal of the Aerospace Sciences*, Vol. 26, No. 9, 1959, pp. 586–591.
doi:10.2514/8.8208.

[33] Brent, R., *Algorithms for Minimization without Derivatives*, chap. 4,5, Prentice-Hall, Englewood Cliffs, NJ, 1973.

[34] Citron, S. J., Dunin, S. E., and Meissinger, H. F., "A Terminal Guidance Technique for Lunar Landing," *AIAA Journal*, Vol. 2, No. 3, 1964, pp. 503 – 509.
doi:10.2514/3.2362.

[35] Cerimele, C., Robertson, E., Sostaric, R., Campbell, C., R. P., Matz, D., Johnson, B., and Stachowiak, S., "A Rigid Mid Lift-to-Drag Ratio Approach to Human Mars Entry, Descent, and Landing," AIAA Paper 2017-1898, 2017.
doi:10.2514/6.2017-1898.